Available online at www.sciencedirect.com
ScienceDirect
International Journal of Heat and Fluid Flow 29 (2008) 579–590
International Journal of HEAT AND FLUID FLOW
www.elsevier.com/locate/ijhff

Large-eddy simulation of supersonic turbulent flow in axisymmetric nozzles and diffusers

Somnath Ghosh [a], Joern Sesterhenn [b], Rainer Friedrich [a,*]

[a] Fachgebiet Strömungsmechanik, Technische Universität München, Boltzmannstr. 15, D-85748 Garching, Germany
[b] Fakultät für Luft- und Raumfahrttechnik, Universität der Bundeswehr München, Werner-Heisenberg-Weg 39, D-85577 Neubiberg/München, Germany

Received 23 October 2007; received in revised form 15 January 2008; accepted 24 January 2008
Available online 2 April 2008

Abstract

Effects of extra strain and dilatation rates on the turbulence structure in nozzles and diffusers with fully developed supersonic pipe flow as inflow condition are investigated by means of LES using high-order numerical schemes. Results from a DNS of pipe and nozzle flow validating the LES are also shown. It is found that weak pressure gradients already strongly inhibit or enhance the Reynolds stresses via corresponding changes of production and pressure–strain terms. The results constitute a database for the improvement of second-order turbulence models for compressible flow.
© 2008 Elsevier Inc. All rights reserved.

Keywords: LES; Compressible wall-bounded flows; Mean dilatation effects

1. Introduction

Compressibility effects in simple turbulent shear flows along isothermal walls, like fully developed channel or pipe flow, manifest themselves in terms of mean density and temperature variations in the near-wall layer and thereby increase the anisotropy of the Reynolds stress tensor. While the peak value of the streamwise Reynolds stress grows with increasing Mach number, the peak values of the other stresses decrease as a consequence of reduced pressure–strain correlations. Since wave-propagation effects are unimportant up to supersonic Mach numbers, solutions of the Poisson equation for the pressure fluctuations by means of a Green function have proven for fully-developed supersonic channel flow (Foysi et al., 2004) that the decrease in mean density from the wall to the channel core is responsible for the decrease of all pressure–strain correlations compared to incompressible flow. Analogous decrease of pressure–strain correlations with increasing Mach number has been observed in pipe flows (Ghosh et al., 2006). Hence, similar mechanisms control the changes in anisotropy of the Reynolds stress transport. They may be summarized as follows. The production of the streamwise Reynolds stress declines with increasing Mach number, but scales with the wall shear stress and the local viscosity along the semi-local wall-normal coordinate. The corresponding pressure–strain correlation does not follow this scaling law, and decreases faster with increasing Mach number which explains the increase in streamwise Reynolds stress. The wall-normal and azimuthal Reynolds stresses have no production terms in their balance equations and decay with increasing Mach number since the pressure–strain correlations decay.

It is to be expected that flows subjected to acceleration and deceleration exhibit even more complex Reynolds stress transport mechanisms. The response of flows to expansion or compression leads to transport phenomena which cannot be explained in terms of mean property variations alone. Bradshaw (1974, 1977) has used the appropriate term 'complex flows' to denote flows in which

* Corresponding author.
E-mail address: r.friedrich@lrz.tum.de (R. Friedrich).

0142-727X/$ - see front matter © 2008 Elsevier Inc. All rights reserved.
doi:10.1016/j.ijheatfluidflow.2008.01.011

significant pressure gradients and strain rates exist. He has discussed the increase in Reynolds stresses by bulk compression and their decrease by bulk expansion in supersonic turbulent boundary layers and has highlighted the need to improve engineering calculation methods. His attempt to account for mean dilatation effects in his empirical Reynolds shear stress equation provides some, but not sufficient improvement in predicting complex compressible flows. In their review article on the physics of supersonic turbulent boundary layers, Spina et al. (1994) stress the need for systematic experimental and DNS data for such complex, compressible flows.

Effects of rapid compression on isotropic turbulence up to an initial turbulent Mach number of $M_t = 0.29$ were studied by Cambon et al. (1993). Using DNS they find turbulence amplification and show that, although there is a rise in pressure-dilatation correlation at higher M_t and at higher compression rates, this is accompanied by an increased turbulent kinetic energy (TKE) production rate through the redistributive pressure–strain correlations. The increase in pressure-dilatation correlation is relatively small compared to that of TKE production. Mahesh et al. (1994) study rapid compression of a shear flow by means of DNS and show that the degree of amplification of TKE and streamwise intensities is higher than in isotropic turbulence. Again, the importance of pressure–strain correlations is confirmed by this study. Effects of rapid expansion on a supersonic turbulent boundary layer have been studied experimentally by Dussauge and Gaviglio (1987). They found that the rapid parts of the pressure–strain correlations are modified and the Reynolds stress decay in the expansion is mainly caused by bulk dilatation production terms (i.e. part of kinetic production) and to a lesser extent by mean pressure gradient production terms (enthalpic production).

While studying the literature, we did not come across systematic numerical investigations of the effects of weak, distributed pressure gradients on compressible, wall-bounded turbulence. Hence, it is our aim to contribute new findings about effects of such weak, distributed dilatation on the turbulence structure in supersonic nozzles and diffusers using well-established and accurate numerical methods. Data presented here from these canonical flow computations could be readily used for further improvement of Reynolds stress closures.

The flow configuration chosen is fully-developed supersonic pipe flow subjected to gradual acceleration/deceleration in a nozzle/diffuser with circular cross-section and isothermal wall. The supersonic pipe flow is driven by a homogeneous body force facilitating the use of streamwise periodicity. Data from this simulation is specified as inflow conditions in real-time to the nozzle/diffuser simulations. Results from large-eddy simulations of these flows using an explicit filtering version of the approximate deconvolution method (ADM) of Stolz et al. (2001) are reported here. A DNS has also been performed to validate the LES data for pipe and nozzle flow.

2. Governing equations and coordinate systems

The governing Navier–Stokes equations are written in a pressure–velocity–entropy form (Sesterhenn, 2001) in generalized curvilinear coordinates:

$$
\begin{aligned}
p_t &= -\frac{\rho c}{2}[X^+ + X^- + Y^+ + Y^- + Z^+ + Z-] \\
&\quad + \frac{p}{C_v}[s_t + X^s + Y^s + Z^s], \\
u_t &= -\frac{\sqrt{g^{11}}}{2}[X^+ - X^-] - Y^u - \frac{g^{21}}{2\sqrt{g^{22}}}[Y^+ - Y^-] \\
&\quad - Z^u - \frac{g^{31}}{2\sqrt{g^{33}}}[Z^+ - Z^-] + \frac{\xi^1_{,i}\xi^l_{,j}}{\rho}\frac{\partial \tau_{ij}}{\partial \xi^l}, \\
v_t &= -X^v - \frac{\sqrt{g^{22}}}{2}[Y^+ - Y^-] - Z^v - \frac{g^{12}}{2\sqrt{g^{11}}}[X^+ - X^-] \\
&\quad - \frac{g^{32}}{2\sqrt{g^{33}}}[Z^+ - Z^-] + \frac{\xi^2_{,i}\xi^l_{,j}}{\rho}\frac{\partial \tau_{ij}}{\partial \xi^l}, \\
w_t &= -X^w - \frac{\sqrt{g^{33}}}{2}[Z^+ - Z^-] - Y^w - \frac{g^{23}}{2\sqrt{g^{22}}}[Y^+ - Y^-] \\
&\quad - \frac{g^{13}}{2\sqrt{g^{11}}}[X^+ - X^-] + \frac{\xi^3_{,i}\xi^l_{,j}}{\rho}\frac{\partial \tau_{ij}}{\partial \xi^l}, \\
s_t &= -X^s - Y^s - Z^s + \frac{1}{\rho T}\left(-\xi^l_i \frac{\partial}{\partial \xi^l}\left(-\lambda \xi^l_i \frac{\partial T}{\partial \xi^l}\right) + \Psi\right). \qquad (1)
\end{aligned}
$$

The coordinates ξ^l are related to the cartesian coordinates x_i by $\frac{\partial}{\partial x_i} = \frac{\partial \xi^l}{\partial x_i}\frac{\partial}{\partial \xi^l}$. $u^1 \equiv u, u^2 \equiv v, u^2 \equiv w$ are the velocities along coordinates $\xi^1 \equiv \xi, \xi^2 \equiv \eta, \xi^3 \equiv \zeta$ and are related to the cartesian velocity components u_i through $u^l = \xi^l_{,i}u_i$. g^{lm} is defined as $g^{lm} = \xi^l_{,i}\xi^m_{,i}$, where $\xi^l_{,i}$ stands for $\frac{\partial \xi^l}{\partial x_i}$. The above equations for the evolution of p, u, v, w and s are solved along with an ideal gas equation of state, $p = \rho RT$, with constant C_p, C_v and constant Prandtl number (Pr). The dynamic viscosity is assumed to vary with temperature according to Sutherland's law: $\mu \propto T^{0.7}$.

$X^\pm, Y^\pm, Z^\pm$ can be interpreted as acoustic waves propagating with velocities $u \pm \sqrt{g^{11}}c$, $v \pm \sqrt{g^{22}}c$ and $w \pm \sqrt{g^{33}}c$ along the curvilinear coordinates ξ^1, ξ^2, ξ^3. X^s, Y^s, Z^s are entropy waves with velocities u, v, and w and $X^{u,v,w}, Y^{u,v,w}, Z^{u,v,w}$ are vorticity waves with corresponding velocities u, v, w, respectively:

$$
\begin{aligned}
X^\pm &\equiv (u \pm \sqrt{g^{11}}c)\left[\frac{p_\xi}{\rho c} \pm \frac{u_\xi}{\sqrt{g^{11}}}\right], \quad X^s \equiv u s_\xi, \\
X^v &\equiv u\left(v_\xi - \frac{g^{12}}{g^{11}}u_\xi\right), \quad X^w \equiv u\left(w_\xi - \frac{g^{13}}{g^{11}}u_\xi\right), \\
Y^\pm &\equiv (v \pm \sqrt{g^{22}}c)\left[\frac{p_\eta}{\rho c} \pm \frac{v_\eta}{\sqrt{g^{22}}}\right], \quad Y^s \equiv v s_\eta, \\
Y^u &\equiv v\left(u_\eta - \frac{g^{21}}{g^{22}}v_\eta\right), \quad Y^w \equiv v\left(w_\eta - \frac{g^{23}}{g^{22}}v_\eta\right),
\end{aligned}
$$

$$Z^{\pm} \equiv (w \pm \sqrt{g^{33}}c)\left[\frac{p_\zeta}{\rho c} \pm \frac{w_\zeta}{\sqrt{g^{33}}}\right], \quad Z^s \equiv w s_\zeta,$$

$$Z^u \equiv w\left(u_\zeta - \frac{g^{31}}{g^{33}} w_\zeta\right), \quad Z^v \equiv w\left(v_\zeta - \frac{g^{32}}{g^{33}} w_\zeta\right).$$

The viscous stress (neglecting bulk viscosity effects), the strain rate tensor and the dissipation rate are defined as

$$\tau_{ij} = 2\mu\left(s_{ij} - \frac{1}{3} s_{kk}\delta_{ij}\right), \quad s_{ij} = \frac{1}{2}\left(\frac{\partial u_i}{\partial x_j} + \frac{\partial u_j}{\partial x_i}\right), \quad \Psi = \tau_{ij} s_{ij}.$$

These equations are solved in an orthogonal (cylindrical) coordinate system for the pipe flow simulations and in a non-orthogonal system for the nozzle/diffuser simulations. The singularity at the axis is avoided by placing no gridpoint on the axis by suitable staggering following Mohseni and Colonius (2000).

Cylindrical coordinates for a domain of length L_x in axial direction and radius R are defined as follows and include the wall-normal tanh stretching:

$$x_1 = \xi L_x, \quad x_2 = \frac{\tanh \kappa\zeta}{\tanh \kappa} R \cos 2\pi\eta, \quad x_3 = \frac{\tanh \kappa\zeta}{\tanh \kappa} R \sin 2\pi\eta,$$

where ξ, η, ζ vary uniformly from 0 to 1 and κ is the stretching factor (κ is taken to be 1.1 in all computations in order to avoid high aspect-ratio of the grid near the centerline).

The non-orthogonal coordinates for the nozzle/diffuser simulations with a domain of length L_x in axial direction and an axially varying radius $f(\xi)$ are defined as follows:

$$x_1 = \xi L_x, \quad x_2 = \frac{\tanh \kappa\zeta}{\tanh \kappa} f(\xi) \cos 2\pi\eta,$$

$$x_3 = \frac{\tanh \kappa\zeta}{\tanh \kappa} f(\xi) \sin 2\pi\eta.$$

$f(\xi)$ is determined in our flow cases using isentropic streamtube equations and specifying a pressure distribution in such a way that the flow goes through an extended region of constant pressure gradient.

3. Numerical method

Sixth-order compact central schemes (Lele, 1992) are used for spatial discretization in the LES. In the DNS, fifth-order compact upwind schemes (Adams and Shariff, 1996) have been used for the convection terms and sixth-order compact central schemes for the molecular transport terms. The flow field is advanced in time in both cases using a third-order low-storage Runge–Kutta scheme (Williamson, 1980).

3.1. LES approach

An explicit filtering variant (Mathew et al., 2003) of the Approximate Deconvolution Method (Stolz et al., 2001) is used for modelling the subgrid scale terms which is briefly explained here using a 1d nonlinear transport equation

$$\frac{\partial u}{\partial t} + \frac{\partial f(u)}{\partial x} = 0.$$

The low-pass filtered transport equation can be written as

$$\frac{\partial \bar{u}}{\partial t} + \frac{\partial f(\bar{u})}{\partial x} = \frac{\partial f(\bar{u})}{\partial x} - G * \frac{\partial f(u)}{\partial x}, \tag{2}$$

where $\bar{u} = G * u = \int G(x - x')u(x')\mathrm{d}x'$ and G is a spatial low-pass filter. Approximate deconvolution $u^* = Q_N * \bar{u}$ uses the approximate inverse of G, $Q_N \approx G^{-1}$ computed using the Van Cittert series, $Q_N = \sum_{n=0}^{N} (I - G)^n$, (Stolz et al., 2001) truncated at $N = 6$ (I is the identity operator).

Eq. (2) can now be written

$$\frac{\partial \bar{u}}{\partial t} + \frac{\partial f(\bar{u})}{\partial x} = \frac{\partial f(\bar{u})}{\partial x} - G * \frac{\partial f(u^*)}{\partial x} + G * \left[\frac{\partial f(u^*)}{\partial x} - \frac{\partial f(u)}{\partial x}\right]. \tag{3}$$

For a useful LES, the low-wavenumber content of the deconvolved field u^* should be as close as possible to that of u, i.e. $G * u^* \approx G * u = \bar{u}$.

The assumption $u = u^*$ gives the simplest LES equation

$$\frac{\partial \bar{u}}{\partial t} + G * \frac{\partial f(u^*)}{\partial x} = 0. \tag{4}$$

A more sophisticated LES equation can be obtained by modelling the square bracket on the RHS of (3) (Mathew et al., 2006). This LES approach is not used here due to its extensive numerical costs. The procedure used to solve (4) involves the following three steps:

$$\text{deconvolution}: \quad u^{*(n)} = Q_N * \bar{u}^n,$$

$$\text{integration}: \quad u^{*(n+1)} \leftarrow u^{*(n)},$$

$$\text{filtering}: \quad \bar{u}^{(n+1)} = G * u^{*(n+1)}.$$

In a simulation, step 1 follows step 3, so that both steps can be combined:

$$u^{*(n)} \leftarrow Q_N * G * u^{*(n)}.$$

Additional regularization by artificial dissipation is found to be necessary in order to mimic the effect of dissipative scales on the resolved scales since the deconvolved variable, u^*, can contain wavenumbers only up to the Nyquist limit of the coarse LES grid. In the ADM formulation of Adams and Leonard (1999) and subsequently in that of Stolz et al. (2001), additional regularization is achieved by adding a relaxation term of the form $\chi(I - Q_N * G) * \bar{u}$ to the filtered equation. A model that is nearly equivalent to a relaxation term is obtained by an additional filtering step with the filter $Q_N * G$ (Mathew et al., 2003). Thus the procedure of deconvolution and regularization is combined here into a single-step filtering with the filter $(Q_N * G)^2$ at each time step.

The filter G used for the periodic directions is a one-parameter Padé filter with $\alpha = 0.2$,

$$\widehat{G}(\omega) = \left(\alpha + \frac{1}{2}\right)\frac{1 + \cos\omega}{1 + 2\alpha\cos\omega}.$$

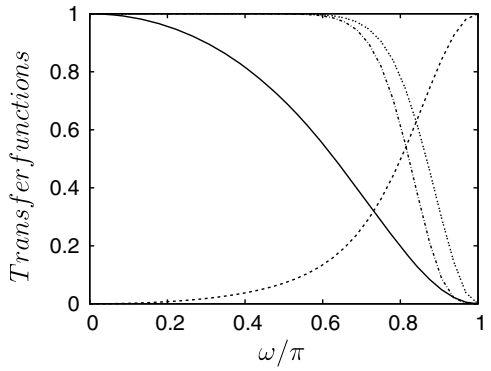

Fig. 1. Transfer functions of filters and their approximate inverse for a periodic case. $\alpha = 0.2$ and $N = 6$: (—) G, (– – –) Q_N, (….) $Q_N * G$, (–·–·–) $(Q_N * G)^2$.

The transfer functions of G, $Q_N * G$, $(Q_N * G)^2$ are shown in Fig. 1.

Ghosh et al. (2006) performed LES of supersonic pipe flow with an isothermal wall using this single-step explicit filtering technique and found very satisfactory agreement with their DNS data concerning correlations that are dominated by large scales.

3.2. Boundary conditions

In the present work, fully-developed supersonic turbulent pipe flow serves as inflow condition for nozzle and diffuser flow. The streamwise periodic pipe flow and the nozzle/diffuser flow simulations are coupled using standard MPI routines (Schlueter et al., 2002). Inflow conditions are specified in the form of characteristics in a similar manner as Poinsot and Lele (1992). In the supersonic region of the inflow plane all the incoming characteristics (X^+, X^-, X^v, X^w, X^s) are specified. In the subsonic region the outgoing acoustic wave X^- is computed from the nozzle flow simulation and this provides acoustic transparency to the inflow. For the viscous terms at the inflow, the streamwise derivatives are computed on a mixed stencil involving points from the pipe and the nozzle/diffuser simulations.

Partially non-reflecting outflow conditions (Poinsot and Lele, 1992) are used in the subsonic region of the outflow plane. The pressure at the outflow is specified by adding a forcing term of the form $X^- = K(p - p_{\text{inf}})$ to the axial momentum equation. This form of forcing brings information into the computational domain about the ambient pressure, p_{inf}. Poinsot and Lele (1992) provide a way to evaluate the constant K such that the imposed condition has only a weak influence on the flow

$$K = \sigma(1 - M^2)c/L,$$

where M is the maximum Mach number in the subsonic flow, L is a characteristic domain size, c is a speed of sound and σ is a constant. In our flow cases, M and c were taken as average quantities, L as the axial domain size and $\sigma = 0.25$.

Extra conditions for the viscous terms are specified by setting to zero the axial derivatives of the transverse shear stresses and the heat flux through the outflow plane

$$\frac{\partial \tau_{12}}{\partial x_1} = 0, \quad \frac{\partial \tau_{13}}{\partial x_1} = 0, \quad \frac{\partial q_1}{\partial x_1} = 0,$$

where x_1 is a coordinate normal to the outflow plane. No sponge layer has been used either in the LES or in the DNS.

At the walls impermeability and no-slip conditions hold and the walls are kept at the same constant temperature in both the pipe and the nozzle/diffuser simulations.

3.3. Computational parameters

We have chosen fully-developed turbulent flow through pipes of constant circular cross-section with isothermal wall as well-defined inflow conditions for the nozzle/diffuser simulations. The working fluid is air with a Prandtl number of 0.7, a ratio of specific heats, $\gamma = 1.4$. The flow is driven by a constant body force. The Mach and the friction Reynolds numbers of the incoming pipe flow for the nozzle computation are 1.5 and 245, while those for the diffuser computation are 1.8 and 280. While the Mach number is based on the speed of sound at wall temperature and bulk velocity, the friction Reynolds number Re_τ is defined using the friction velocity $u_\tau = \sqrt{\tau_w/\rho_w}$, the pipe radius R and the kinematic viscosity at the wall, $\nu_w(T_w)$. The domain length of each configuration (pipe or nozzle/diffuser) is $L = 10R$. The streamwise variation of the flow cross-section is calculated using streamtube equations for a given streamwise pressure distribution. This is done to ensure that the turbulence is subjected to an extended region of nearly constant weak pressure gradient. The Clauser pressure gradient parameter, $\beta = \frac{\delta^*}{\tau_w}\frac{d\bar{p}}{dx}$, has an average value of -1.6 in the nozzle and 1.6 in the diffuser, respectively. The ratios of nozzle- and diffuser radii to pipe radius at the ends of the computational domains are 1.58 (nozzle) and 0.93 (diffuser). The number of grid points used to discretize the pipe and nozzle domains are $64 \times 64 \times 50$ in the LES and $256 \times 128 \times 91$ in the DNS in streamwise, circumferential and radial directions. For the LES of diffuser flow, a grid of $64 \times 64 \times 50$ points is chosen as well.

4. Results

Results are presented in three sections. The first section is dedicated to fully-developed supersonic pipe flow that serves as inflow condition for nozzle and diffuser flow. In the second section, we discuss mean flow features in the nozzle, the evolution of Reynolds stresses and Reynolds stress budgets with a focus on pressure–strain correlations and the various contributions to production. Most of the results are based on LES data. DNS data are occasionally used to validate the results. The third section concentrates on analogous effects in the diffuser. Here, only LES data are available.

4.1. Fully-developed supersonic pipe flow

We focus here on the inflow conditions for nozzle flow alone, as an example, since they are similar to those of diffuser flow. The computational domain for the pipe is $10R \times 2\pi R \times R$ where R is the pipe radius. The pipe wall is kept isothermal. For the DNS $256 \times 128 \times 91$ points are used in the streamwise, azimuthal and radial directions while the LES was carried out with $64 \times 64 \times 50$ points. Table 1 summarizes the computational parameters.

In order to check how the LES performs, we plot energy spectra in the peak TKE production zone (Fig. 2) of the three velocity fluctuations versus streamwise wavenumbers normalized using local friction velocity $u_\tau^* = \sqrt{\tau_w/\bar{\rho}}$ and local kinematic viscosity $\bar{\nu}$. Careful observation reveals a slight overshoot of the LES spectra over the DNS spectra for the axial (u_x) and azimuthal (u_ϕ) large-scale components and a slight undershoot over a broad range in the radial component (u_r).

In what follows we present comparisons between DNS and LES data for some mean flow quantities and the normal and shear Reynolds stress components. Fig. 3 shows the mean velocity profile in Van Driest scaling

$$U_{\mathrm{VD}}^+ : \int_0^{\bar{u}_x{}^+} \sqrt{\frac{\bar{\rho}}{\bar{\rho}_w}}\, \mathrm{d}\bar{u}_x{}^+$$

versus the wall coordinate $y^+ = y u_\tau / \nu_w$. The fact that the profile deviates remarkably from the standard log-law $u^+ = 2.5 \ln y^+ + 5.5$ is due to the relatively low Reynolds number $Re_\tau = 245$. An increase in Re_τ moves the profile closer to the log-law (not shown here).

Table 1
Flow and computation parameters

Case	Δx^+	$r\Delta\phi^+_{\max}$	$\Delta r^+_{\min}$	$\Delta r^+_{\max}$	M	Re_τ	T_w
DNSM1.5	9.5	12.0	1.3	3.73	1.5	245	220
LESM1.5	38	21.2	2.5	6.79	1.5	244	220

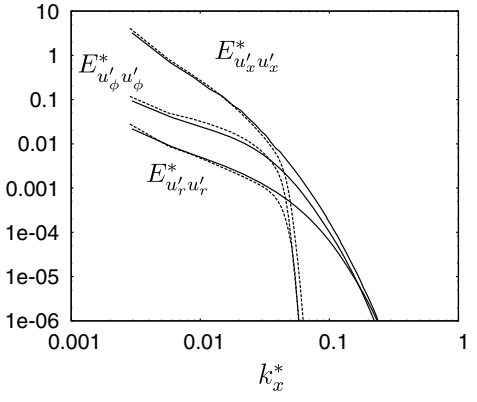

Fig. 2. Streamwise energy spectra, averaged in the azimuthal direction for the three velocity components in the buffer layer ($y^+ = 20$). Solid line: DNS, dashed line: LES.

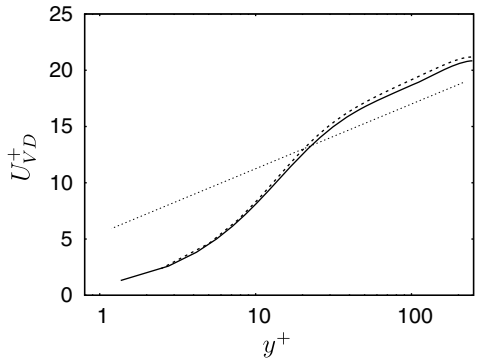

Fig. 3. Van Driest transformed velocity. Solid line: DNS; dashed line: LES. Dotted line: $u^+ = 2.5 \ln y^+ + 5.5$.

As seen in Fig. 4, the streamwise Reynolds stress $\overline{\rho u_x'' u_x''}/\tau_w$ is slightly overpredicted by the LES in the buffer layer where the production of TKE peaks. In that zone, the radial Reynolds stress reveals an underprediction in the LES. Both effects appear to be consistent with those found in the corresponding energy spectra and they compensate each other in the Reynolds shear stress (Fig. 5). We conclude this subsection with results for the mean temperature, mean density and mean pressure in Figs. 6 and 7. All the LES results show marginal differences from the DNS

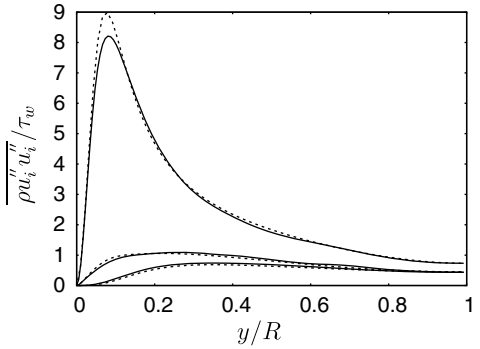

Fig. 4. Normal Reynolds stresses, normalized with wall shear stress. Solid line: DNS; dashed line: LES.

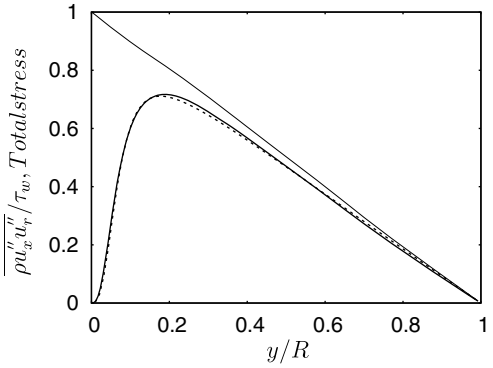

Fig. 5. Reynolds shear stress and total stress, normalized with wall shear stress. Solid line: DNS; dashed line: LES.

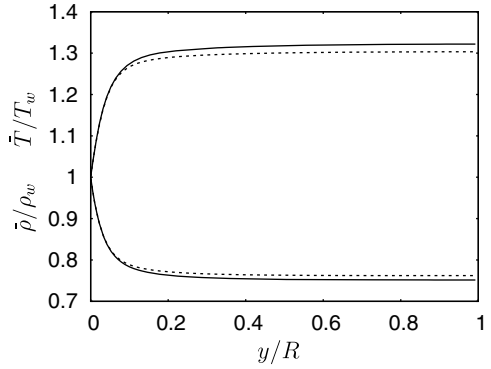

Fig. 6. Mean temperature and density profiles. Solid lines: DNS; dashed lines: LES.

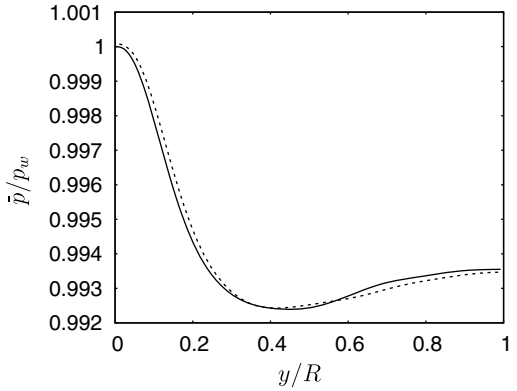

Fig. 7. Mean pressure profiles. Solid lines: DNS; dashed lines: LES.

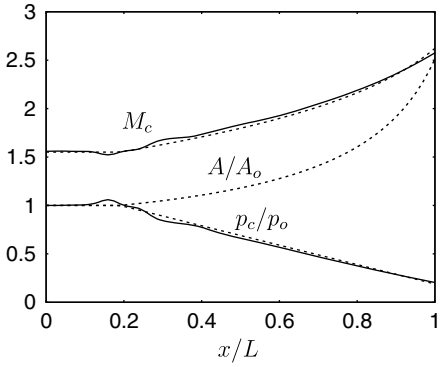

Fig. 8. Streamwise variation of cross-sectional area (A), mean centerline Mach number (M_c) and pressure (p_c) in the nozzle. (—) LES, (– – –) Isentropic streamtube. Subscript 'o' denotes value at inflow $x/L = 0$.

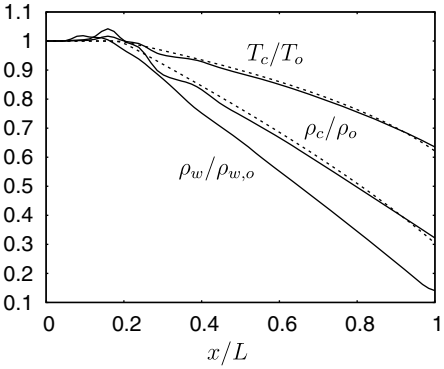

Fig. 9. Streamwise variation of mean centerline density (ρ_c), wall density (ρ_w) and centerline temperature (T_c) in the nozzle. (—) LES, (– – –) Isentropic streamtube. Subscript 'o' denotes value at inflow $x/L = 0$.

results. An interesting physical aspect should be noted in Fig. 7. The radial pressure variations are so low that they can be neglected with respect to the strong mean temperature variations. As a result, the mean ideal gas law predicts a close radial coupling between mean temperature and density fields.

4.2. Nozzle flow

For an improved understanding of compressibility and acceleration effects it is necessary to discuss the behaviour of mean primitive flow variables first. Fig. 8 contains axial profiles of mean centerline Mach number and pressure (normalized with their values at the inflow). Fig. 8 also presents the axial variation of the nozzle cross-section A, normalized with its upstream value, A_o. A starts increasing at $x/L = 0.16$, after a short section of constant diameter. When A has reached its maximum value of 2.5, the centerline Mach number has increased from 1.52 to 2.5 which represents a factor of 1.64 increase. Fig. 9 shows profiles of mean temperature and density along the nozzle centerline. In both figures results obtained from isentropic streamtube equations have been plotted for comparison. Since viscous effects are of little importance in the core region of the nozzle, the flow behaves close to the accelerated isentropic flow with decreasing pressure, density and temperature. Of course, we cannot expect full agreement between the real flow and the streamtube results, because streamline curvature, which sets in at $x/L \approx 0.1$ affects the near-wall turbulence activity and, in turn, also the flow and the thermodynamic variables on the axis. The wall shear stress first shows an increase and a subsequent slow decrease (Fig. 10). It should be noted that the abrupt jump in the wall shear stress near the outflow is a consequence of the outflow boundary condition which, however, remains local. In what follows, τ_w is used for normalization at positions $x/L = 0.0$, 0.45, and 0.8. At these downstream positions, τ_w is obviously larger than in the pipe, as a result of acceleration.

Fig. 11 presents the streamwise evolution of radial mean temperature and density profiles and a comparison of DNS and LES data, which proves good agreement. In fully developed pipe flow ($x/L = 0.0$) mean density and temperature are directly linked in radial direction, since the radial pressure gradient is negligibly small. The heat generated by dissipation in the wall layer strongly increases the mean temperature and leads to a heat flux out of the pipe. The mean density in turn drops from its high wall value to a low core value and thus reduces the pressure–strain corre-

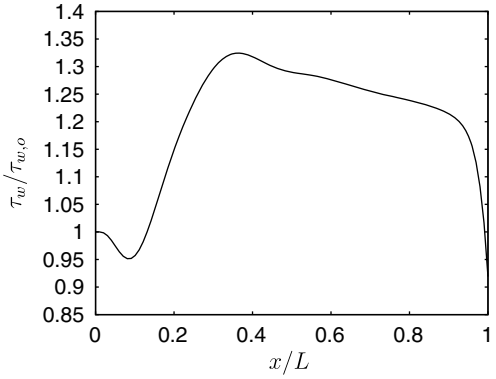

Fig. 10. Wall shear stress along the nozzle (LES). Subscript 'o' denotes value at inflow $x/L = 0$.

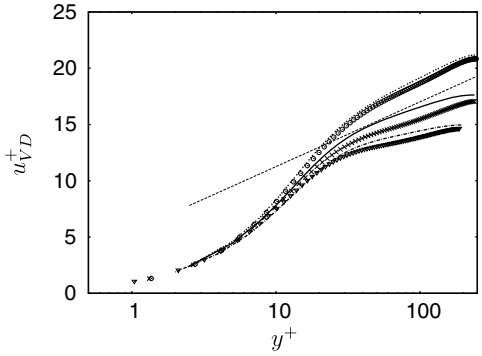

Fig. 12. Van Driest transformed mean velocity profiles in the nozzle in wall coordinates. x/L stations as in Fig. 11. Lines: LES, symbols: DNS. Straight line: $2.5 \ln y^+ + 5.5$.

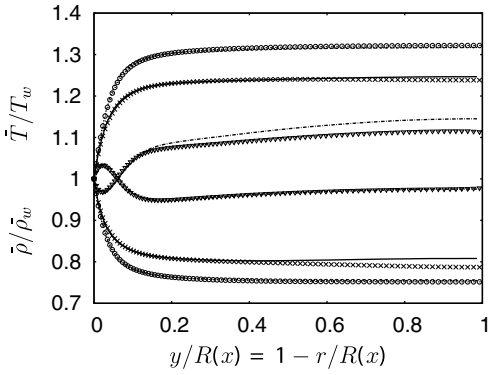

Fig. 11. Mean density and temperature profiles in the nozzle at stations $x/L = 0.0(\ldots\ \ldots)$, 0.45 (—), 0.8 (–·–·–). Lines: LES, symbols: DNS.

lations. This effect, explained for turbulent channel flow by Foysi et al. (2004), also holds for pipe flow, (Ghosh et al., 2006). The described direct coupling between temperature and density in radial direction persists in the present accelerated flow (Fig. 11, $x/L > 0.0$). While in the nozzle core adiabatic cooling due to acceleration compensates dissipative heating and hence leads to a downstream decreasing ratio $\bar{T}/T_w$, this effect is less pronounced in the near-wall region. The fact that $\bar{\rho}/\bar{\rho_w}$ increases with x/L is counterintuitive. It is due to the thermal boundary condition (isothermal wall) and to the fact that the wall density decreases proportional to the wall pressure and obviously faster than the mean density on the centerline (Fig. 9). Due to flow acceleration in the nozzle the mean sonic line moves closer to the wall, so that the layer in which subsonic flow persists gets thinner in downstream direction. The strong increase in wall shear stress due to acceleration and the weaker increase in mean density ratio combine in such a way that the Van Driest transformed velocity profiles develop as shown in Fig. 12. Similar effects in the velocity profiles were observed by Bae et al. (2006) in DNS of strongly heated low-speed air flow in pipes of constant diameter. There the flow is accelerated because the bulk density decreases nearly linearly within a certain section of constant wall-heating. In the case of strong wall-heating (run 445 of Bae et al., 2006), the Van Driest transformed velocity profiles fall below the universal shape, like in the present nozzle flow. However, it should be noted that the streamwise temperature profiles are different in the two flow cases.

Flow acceleration dramatically affects the turbulence structure. An instantaneous plot of axial velocity fluctuations (Fig. 13) shows that the turbulence activity near the wall is gradually reduced as we proceed downstream. However, we note that the flow near the outflow is not relaminarized. The streamwise Reynolds stress, normalized with the local wall shear stress, decreases by nearly an order of magnitude, as seen in Fig. 14. Due to non-equilibrium of the flow, τ_w is no longer a suitable scaling parameter

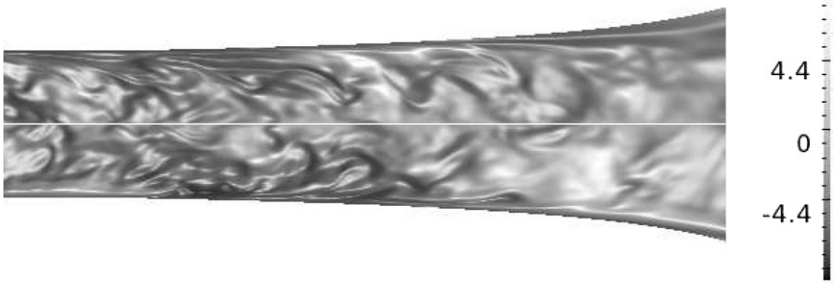

Fig. 13. Axial velocity fluctuations, normalized with $\sqrt{\tau_w/\rho_w}|_o$, in a (x, r)-plane of the nozzle (DNS).

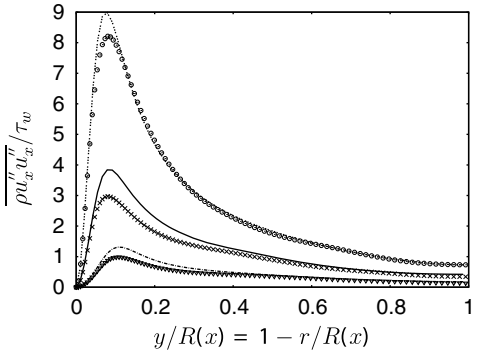

Fig. 14. Streamwise Reynolds stress in the nozzle normalized with the local wall shear stress. Lines: LES, symbols: DNS. x/L stations as in Fig. 11.

for collapsing Reynolds stress profiles in the core region, as it is for fully-developed pipe flow (Ghosh et al., 2006). Fig. 15 presents the downstream evolution of the Reynolds shear stress and the total shear stress. Here again, a dramatic decrease of all terms in the flow direction is observed. Finally, a strong decay of the solenoidal TKE dissipation rate and a decrease of the peak value of the turbulent Mach number from 0.25 to 0.17 are observed in this flow (not shown here for brevity).

In order to understand the reasons for these changes in the nozzle, we examine production terms and pressure–strain correlations in the Reynolds stress budgets of $\overline{\rho u_x'' u_x''}/2$, $\overline{\rho u_x'' u_r''}$, $\overline{\rho u_r'' u_r''}/2$ and express them in a cylindrical (x, ϕ, r)-coordinate system which differs only weakly from the computational coordinate system. In such a system the radial budget contains production terms as well. We distinguish between 'kinetic' and 'enthalpic' production and split, following Gaviglio et al. (1977), the first into contributions due to shear, extra rate of strain and mean dilatation. It should be noted that production by mean dilatation is the only explicit compressibility effect, since production by shear and extra rate of strain appear also in incompressible pipe flow with varying cross-section.

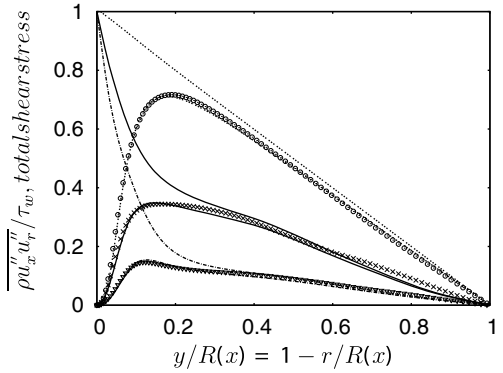

Fig. 15. Reynolds shear stress and total shear stress in the nozzle normalized with the local wall shear stress. Lines: LES, symbols: DNS. x/L stations as in Fig. 11.

The 'kinetic' production terms in the nozzle (and diffuser) flow without swirl are

$$P_{xx} = \underbrace{-\overline{\rho u_x'' u_r''}\frac{\partial \widetilde{u}_x}{\partial r}}_{\text{shear}} \underbrace{-\frac{1}{3}\overline{\rho u_x'' u_x''}\frac{\partial \widetilde{u}_l}{\partial x_l}}_{\text{mean dilatation}} \underbrace{-\overline{\rho u_x'' u_x''}\left(\frac{\partial \widetilde{u}_x}{\partial x} - \frac{1}{3}\frac{\partial \widetilde{u}_l}{\partial x_l}\right)}_{\text{extra rate of strain}}$$

$$P_{xr} = \underbrace{-\overline{\rho u_r'' u_r''}\frac{\partial \widetilde{u}_x}{\partial r}}_{\text{shear1}} \underbrace{-\overline{\rho u_x'' u_x''}\frac{\partial \widetilde{u}_r}{\partial x}}_{\text{shear2}} \underbrace{-\frac{2}{3}\overline{\rho u_x'' u_r''}\frac{\partial \widetilde{u}_l}{\partial x_l}}_{\text{mean dilatation}} \underbrace{-\overline{\rho u_x'' u_r''}\left(\frac{\partial \widetilde{u}_x}{\partial x} + \frac{\partial \widetilde{u}_r}{\partial r} - \frac{2}{3}\frac{\partial \widetilde{u}_l}{\partial x_l}\right)}_{\text{extra rate of strain}}$$

$$P_{rr} = \underbrace{-\overline{\rho u_x'' u_r''}\frac{\partial \widetilde{u}_r}{\partial x}}_{\text{shear}} \underbrace{-\frac{1}{3}\overline{\rho u_r'' u_r''}\frac{\partial \widetilde{u}_l}{\partial x_l}}_{\text{mean dilatation}} \underbrace{-\overline{\rho u_r'' u_r''}\left(\frac{\partial \widetilde{u}_r}{\partial r} - \frac{1}{3}\frac{\partial \widetilde{u}_l}{\partial x_l}\right)}_{\text{extra rate of strain}}$$

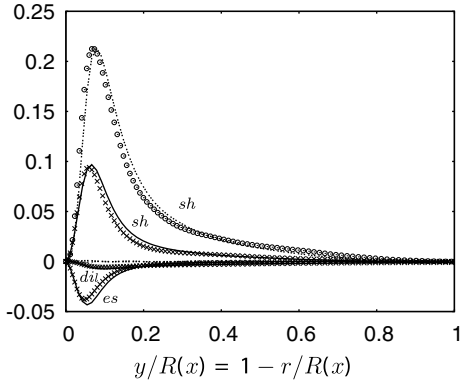

Fig. 16. Contributions to production of the axial Reynolds stress in the nozzle at stations $x/L = 0.0$ (dotted line) and 0.45 (solid line). sh: mean shear, dil: mean dilatation, es: extra rate of strain. Lines: LES, symbols: DNS. All terms are normalized by $\tau_w^2/\bar{\mu}$.

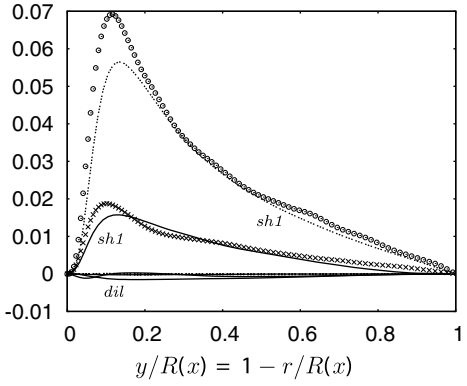

Fig. 17. Contributions to production of the Reynolds shear stress in the nozzle at stations $x/L = 0.0$ (dotted line), 0.45 (solid line). sh1: mean shear (*shear1*), dil: mean dilatation. Lines: LES, symbols: DNS. All terms are normalized by $\tau_w^2/\bar{\mu}$.

Figs. 16 and 17 show the contributions to P_{xx} and P_{xr} in the nozzle at $x/L = 0.45$ and in fully-developed pipe flow (which corresponds to the position $x/L = 0$), normalized with local values of $\tau_w^2/\bar{\mu}$. Among the two production by shear terms in P_{xr}, the first is dominant and the second is negligible in this specific nozzle. Clearly, compressibility in the form of mean dilatation counteracts the shear production of the $\overline{\rho u_x'' u_x''}$, $\overline{\rho u_x'' u_r''}$ components. Production by acceleration (extra rate of strain) does the same, at least in the streamwise component. The production rates by shear are themselves reduced by the stabilization of the two stresses $\overline{\rho u_x'' u_r''}$ and $\overline{\rho u_r'' u_r''}$. Again, good agreement is found between the DNS and LES results. In the $\overline{\rho u_x'' u_x''}$-budget enthalpic production appears on the RHS in the form $-\overline{u_x''}\frac{\partial \bar{p}}{\partial x}$ and has only a very small positive value (not shown).

The pressure–strain correlations can be split into deviatoric and dilatational parts

$$\Pi_{xx} = \overline{p'\left(\frac{\partial u_x''}{\partial x} - \frac{d'}{3}\right)} + \frac{1}{3}\overline{p'd'},$$

$$\Pi_{xr} = \overline{p'\left(\frac{\partial u_r''}{\partial x} + \frac{1}{r}\frac{\partial r u_x''}{\partial r}\right)},$$

$$\Pi_{rr} = \overline{\frac{1}{r}p'\left(\frac{\partial r u_r''}{\partial r} - \frac{d'}{3}\right)} + \frac{1}{3}\overline{p'd'}.$$

d' represents dilatational fluctuations. Profiles of Π_{xx}, Π_{xr}, normalized with local values of $\tau_w^2/\bar{\mu}$, are presented in Figs. 18 and 19 for stations $x/L = 0.0, 0.45, 0.8$. The dramatic reduction of the deviatoric parts in the nozzle is obvious. The contribution of the pressure-dilatation correlation is very small. Besides the weak production by shear, the Π_{rr}-term is the only source term in the radial stress budget. The streamwise decay of $\overline{\rho u_r'' u_r''}$ is therefore mainly due to the reduction of the pressure–strain correlation which can be traced back to the reduction of pressure and velocity-gradient fluctuations. It remains to be shown which role mean dilatation, extra strain rate and mean density variation play in damping pressure fluctuations.

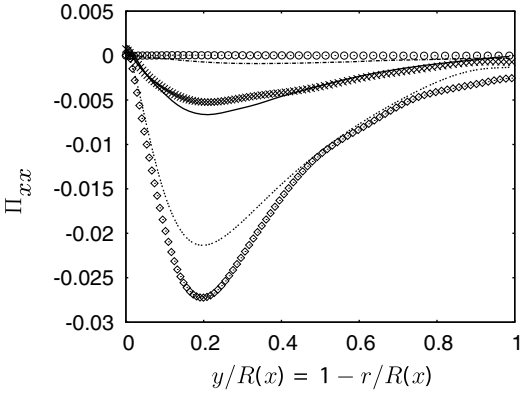

Fig. 18. Pressure–strain correlation Π_{xx} in the nozzle. Lines: LES at $x/L = 0.0(\ldots\ \ldots)$, 0.45 (—), 0.8 (–·–·–). (◇), (×): Π_{xx} (DNS) at $x/L = 0, 0.45$, respectively. (⊙), $\overline{p'd'/3}$ (LES) at $x/L = 0.45$. Terms are normalized by $\tau_w^2/\bar{\mu}$.

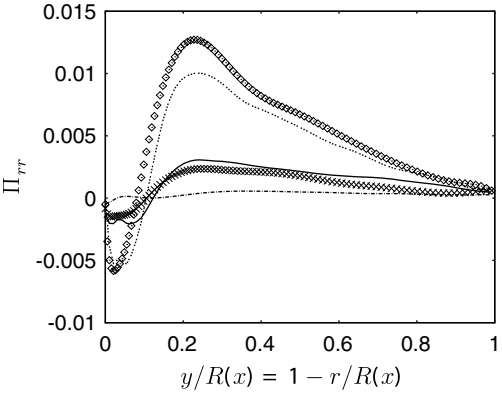

Fig. 19. Pressure–strain correlation Π_{rr} in the nozzle. Lines: LES at $x/L = 0.0$ $(\ldots\ \ldots)$, 0.45 (—), 0.8 (–·–·–). (◇), (×): Π_{rr} (DNS) at $x/L = 0, 0.45$, respectively. Terms are normalized by $\tau_w^2/\bar{\mu}$.

4.3. Diffuser flow

Supersonic turbulent diffuser flow is not just the opposite of nozzle flow. Its behaviour strongly depends on the rate of deceleration, and the Mach and Reynolds numbers at the inlet. We recall that the inlet Mach and friction Reynolds numbers are 1.8 and 280. The chosen higher incoming Mach and Reynolds numbers (they are 1.5 and 250 for nozzle flow) avoid noticeable transonic regions at the end of the diffuser. Moreover, the axial profiles of centerline Mach number and pressure (Fig. 20), as well as centerline density and temperature (Fig. 21) do not follow predictions of the isentropic streamtube equations. Wall and centerline pressure, density and temperature distributions grow much faster due to trains of compression and expansion waves reminding us of shock trains observed in experiments at stronger flow deceleration (Matsuo et al., 1999). The wall shear stress in this flow first decreases and subsequently increases, see Fig. 22. At positions $x/L = 0.2$, 0.45 where flow conditions are investigated below, it is remarkably lower than at the inflow plane ($x/L = 0.0$) which corresponds to fully-developed pipe flow.

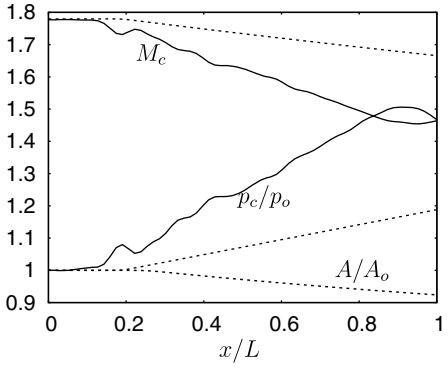

Fig. 20. Axial variation of cross-sectional area, mean centerline Mach number and pressure in the diffuser. (—) LES, (–––) Isentropic streamtube. Subscript 'o' denotes value at inflow $x/L = 0$.

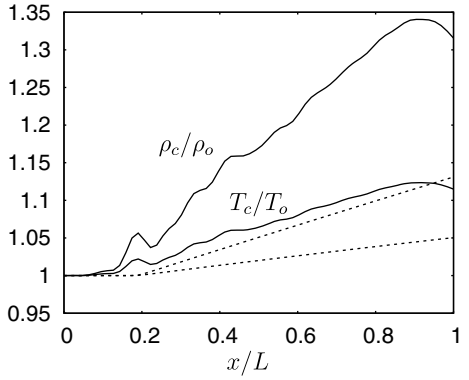

Fig. 21. Axial variation of mean centerline density and temperature in the diffuser. (—) LES, (– – –) Isentropic streamtube. Subscript 'o' denotes value at inflow $x/L = 0$.

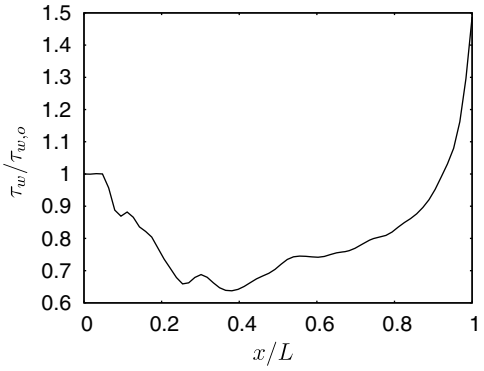

Fig. 22. Wall shear stress along the diffuser. Subscript 'o' denotes value at inflow $x/L = 0$.

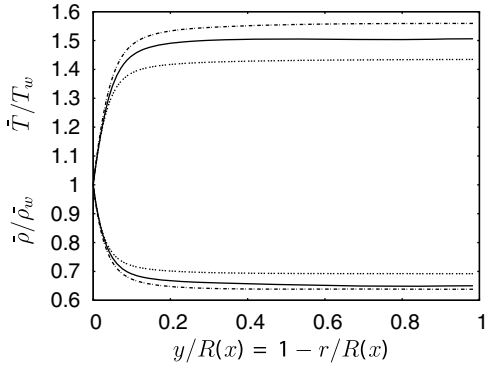

Fig. 23. Mean density and temperature profiles in the diffuser at stations $x/L = 0.0(\ldots\ \ldots)$, 0.2 (—), 0.45 (–·–·–).

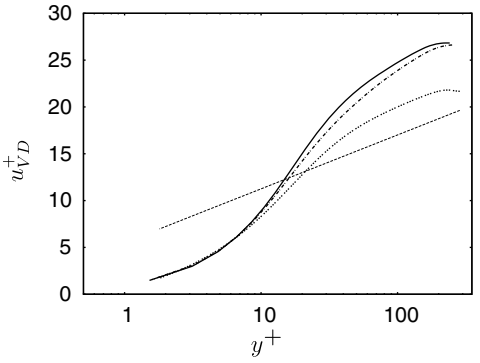

Fig. 24. Van Driest transformed mean velocity profiles in the diffuser in wall coordinates. x/L stations as in Fig. 23. Straight line: $2.5\ln y^+ + 5.5$.

Fig. 23 reveals that the mean temperature grows in the diffuser in flow direction due to compression and increased dissipation rate (not shown). As a consequence the mean density ratio decays in flow direction. The Van Driest transformed mean axial velocity now reaches levels higher than in fully developed pipe flow, see Fig. 24. This is predominantly a result of the streamwise reduction of wall shear stress. Increased turbulence activity in the near-wall region of the diffuser is observed in the plot of instantaneous axial velocity fluctuations (Fig. 25) The Reynolds stresses provide the proof of the enhanced turbulence activity. As an example we show the streamwise Reynolds stress in Fig. 26 and the total as well as Reynolds shear stress in Fig. 27. Although the flow deceleration is fairly weak (the centerline Mach number decreases from 1.8 to 1.45) the Reynolds stresses increase by roughly a factor of 2. As a typical sign of decelerated wall-bounded flow, the maximum shear stress increases in magnitude and moves away from the wall. We also note a growth in the solenoidal dissipation rate and the turbulent Mach number and are aware that an LES can predict trends of turbulent dissipation rates reliably, but not their absolute values. The enhanced turbulence activity is reflected in the production of Reynolds stresses by mean shear, extra rate of strain and mean dilatation. Fig. 28 shows that, in contrast to the nozzle flow, mean dilatation and extra rates of strain now act as sources producing streamwise Reynolds stress. The first production by shear term (Fig. 29) in the shear

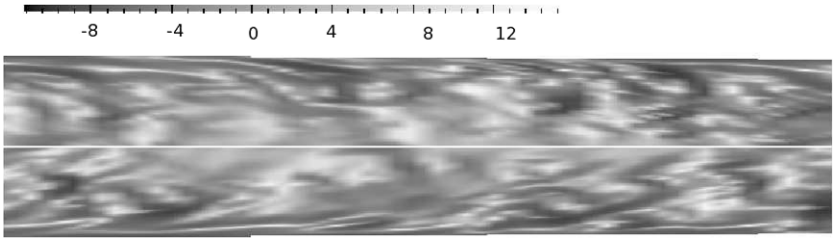

Fig. 25. Axial velocity fluctuations, normalized with $\sqrt{\tau_w/\rho_w}|_o$, in a (x,r)-plane of the diffuser (LES).

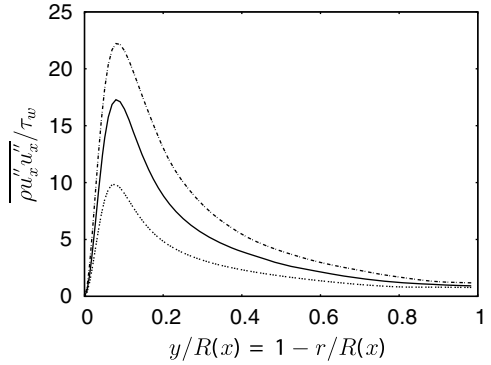

Fig. 26. Streamwise Reynolds stress in the diffuser normalized with the local wall shear stress. x/L stations as in Fig. 23.

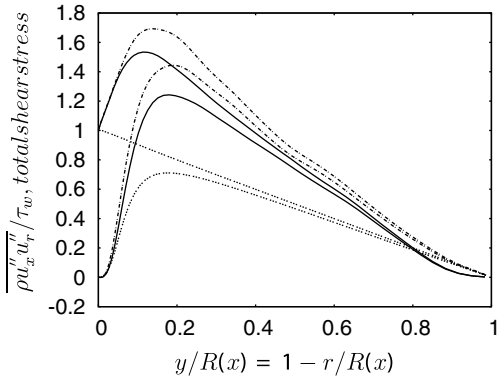

Fig. 27. Reynolds shear stress and total shear stress in the diffuser normalized with the local wall shear stress. x/L stations as in Fig. 23.

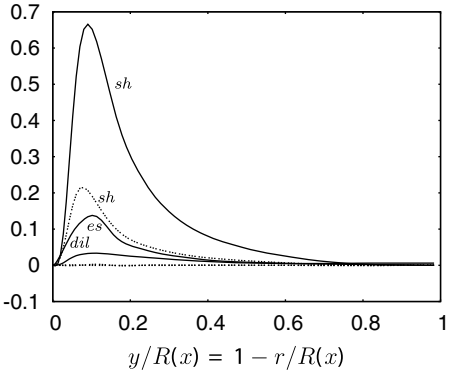

Fig. 28. Contributions to production of the axial Reynolds stress in the diffuser at stations $x/L = 0.0$ (dotted line) and 0.2 (solid line). sh: mean shear, dil: mean dilatation, es: extra rate of strain. All terms are normalized by $\tau_w^2/\bar{\mu}$.

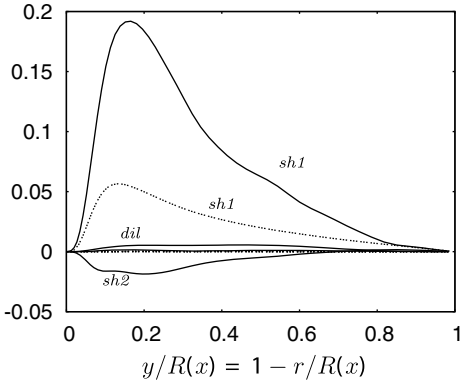

Fig. 29. Contributions to production of the Reynolds shear stress in the diffuser at stations $x/L = 0.0$ (dotted line), 0.2 (solid line). sh1: mean shear (*shear1*), sh2: mean shear (*shear2*), dil: mean dilatation. All terms are normalized by $\tau_w^2/\bar{\mu}$.

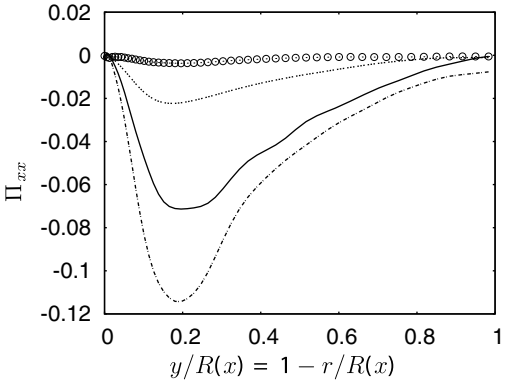

Fig. 30. Pressure–strain correlation Π_{xx} in the diffuser. x/L stations as in Fig. 23. ($\odot$), $\overline{p'd'}/3$ at $x/L = 0.2$. Terms are normalized by $\tau_w^2/\bar{\mu}$.

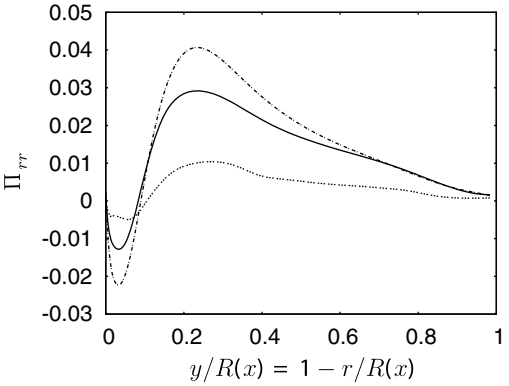

Fig. 31. Pressure–strain correlation Π_{rr} in the diffuser. x/L stations as in Fig. 23. Terms are normalized by $\tau_w^2/\bar{\mu}$.

stress equation increases in a similar fashion as it decreases in the supersonic nozzle. The second term of this kind is now non-zero, but counteracts the first. Mean dilatation has a weak source effect on turbulence production. Finally, the pressure–strain correlations grow in decelerated flow and provide increased contributions to the radial and circumferential Reynolds stress components. The peak of the axial pressure–strain correlation in Fig. 30 grows by a factor of at least five in the domain considered. The pressure-dilatation correlation taken at $x/L = 0.2$ is still very small compared to Π_{xx}. The axial growth of the radial pressure–strain correlation (Fig. 31), explains the growth of the radial Reynolds stress in the diffuser.

5. Conclusions

Supersonic turbulent pipe flow subjected to gradual acceleration/deceleration in a nozzle/diffuser has been investigated by means of LES in order to assess the effects of mean dilatation and extra rate of strain on the turbulence structure. Occasionally, DNS has been used to validate the LES results. Although the rates of acceleration/deceleration and mean dilatation are small, the decrease/increase in Reynolds stress components is large. At the same time dilatational fluctuations are only weakly affected, so that explicit compressibility terms (like pressure-dilatation and compressible dissipation rate) remain small. While extra rates of strain and mean dilatation act as small source/sink terms in the Reynolds stress transport equations, the strong modification of production due to shear caused by large changes in pressure–strain correlations is the major cause of decay/amplification of Reynolds stresses in these flows. It remains to be shown in which way extra-rates of strain, mean dilatation and mean density variations affect pressure and velocity-gradient fluctuations and thus control the variation of pressure–strain correlations. This is the aim of future work.

References

Adams, N.A., Leonard, A., 1999. Deconvolution of subgrid scales for the simulation of shock-turbulence interaction. In: Voke, P., Sandham, N.D., Kleiser, L. (Eds.), Direct and Large-Eddy Simulation III. p. 201.

Adams, N.A., Shariff, K., 1996. A high-resolution hybrid compact-ENO scheme for shock-turbulence interaction problems. Journal of Computational Physics 127, 27–51.

Bae, J.H., Yoo, J.Y., Choi, H., McEligot, D.M., 2006. Effects of large density variation on strongly heated internal air flows. Physics of Fluids, 18.

Bradshaw, P., 1974. The effect of mean compression or dilatation on the turbulence structure of supersonic boundary layers. Journal of Fluid Mechanics 63, 449–464.

Bradshaw, P., 1977. Compressible turbulent shear layers. Annual Review of Fluid Mechanics 9, 33–52.

Cambon, C., Coleman, G.N., Mansour, N.N., 1993. Rapid distortion analysis and direct simulation of compressible homogeneous turbulence at finite mach numbers. Journal of Fluid Mechanics 257, 641–665.

Dussauge, J.P., Gaviglio, J., 1987. The rapid expansion of a supersonic turbulent flow: role of bulk dilatation. Journal of Fluid Mechanics 174, 81–112.

Foysi, H., Sarkar, S., Friedrich, R., 2004. Compressibility effects and turbulence scalings in supersonic channel flow. Journal of Fluid Mechanics 509, 207–216.

Gaviglio, J., Dussauge, J., Debieve, J., Favre, A., 1977. Behaviour of a turbulent flow, strongly out of equilibrium at supersonic speeds. Physics of Fluids 20 (10), 179–192.

Ghosh, S., Sesterhenn, J., Friedrich, R., 2006. DNS and LES of Compressible Turbulent Pipe Flow with Isothermal Wall. Direct and large eddy simulation VI. Springer.

Lele, S., 1992. Compact finite difference schemes with spectral-like resolution. Journal of Computational Physics 103, 16–42.

Mahesh, K., Lele, S.K., Moin, P., 1994. The response of anisotropic turbulence to rapid homogeneous one-dimensional compression. Physics of Fluids 6 (2), 1062.

Mathew, J., Lechner, R., Foysi, H., Sesterhenn, J., Friedrich, R., 2003. An explicit filtering method for large eddy simulation of compressible flows. Physics of Fluids 15, 2279–2289.

Mathew, J., Foysi, H., Friedrich, R., 2006. A new approach to LES based on explicit filtering. International Journal of Heat and Fluid Flow 27, 594–602.

Matsuo, K., Miyazato, Y., Kim, H., 1999. Shock train and pseudo-shock phenomena in internal gas flows. Progress in Aerospace Sciences 35, 33–100.

Mohseni, K., Colonius, T., 2000. Numerical treatment of polar coordinate singularities. Journal of Computational Physics 157, 787–795.

Poinsot, T.J., Lele, S.K., 1992. Boundary conditions for direct simulations of compressible viscous flows. Journal of Computational Physics 101, 104–129.

Schlueter, J.U., Shankaran, S., Kim, S., Pitsch, H., Alonso, J.J., 2002. Integration of RANS and LES flow solvers: interface validation. Annual Research Briefs, CTR, Stanford, pp. 155–166.

Sesterhenn, J., 2001. A characteristic-type formulation of the Navier–Stokes equations for high order upwind schemes. Computers and Fluids 30, 37–67.

Spina, E.F., Smits, A.J., Robinson, S.K., 1994. The physics of supersonic turbulent boundary layers. Annual Review of Fluid Mechanics 26, 287–319.

Stolz, S., Adams, N.A., Kleiser, L., 2001. An approximate deconvolution model for large-eddy simulation with application to incompressible flows. Physics of Fluids 13, 997–1015.

Williamson, J.K., 1980. Low-storage Runge–Kutta schemes. Journal of Computational Physics 35, 48–56.